

Unsupervised Density Neural Representation for CT Metal Artifact Reduction

Qing Wu, Xu Guo, Lixuan Chen, Dongming He, Hongjiang Wei, Xudong Wang, S. Kevin Zhou, *Fellow, IEEE*, Yifeng Zhang, Jingyi Yu, *Fellow, IEEE*, and Yuyao Zhang, *Member, IEEE*

Abstract—Emerging unsupervised reconstruction techniques based on implicit neural representation (INR), such as NeRP, CoIL, and SCOPE, have shown unique capabilities in CT linear inverse imaging. In this work, we propose a novel unsupervised density neural representation (Diner) to tackle the challenging problem of CT metal artifacts when scanned objects contain metals. The drastic variation of linear attenuation coefficients (LACs) of metals over X-ray spectra leads to a nonlinear beam hardening effect (BHE) in CT measurements. Recovering CT images from metal-affected measurements therefore poses a complicated nonlinear inverse problem. Existing metal artifact reduction (MAR) techniques mostly formulate the MAR as an image inpainting task, which ignores the energy-induced BHE and produces suboptimal performance. Instead, our Diner introduces an energy-dependent polychromatic CT forward model to the INR framework, addressing the nonlinear nature of the MAR problem. Specifically, we decompose the energy-dependent LACs into energy-independent densities and energy-dependent mass attenuation coefficients (MACs) by fully considering the physical model of X-ray absorption. Using the densities as pivot variables and the MACs as known prior knowledge, the LACs can be accurately reconstructed from the raw measurements. Technically, we represent the unknown density map as an implicit function of coordinates. Combined with a novel differentiable forward model simulating the physical acquisition from the densities to the measurements, our Diner optimizes a multi-layer perception network to approximate the implicit function by minimizing predicted errors between the estimated and real measurements. Experimental results on simulated and real datasets confirm the superiority of our unsupervised Diner against popular supervised techniques in MAR performance and robustness. To the best of

our knowledge, our Diner is the first unsupervised MAR method that significantly outperforms its supervised counterparts.

Index Terms—X-ray CT, Metal Artifact Reduction, Neural Representation, Unsupervised Learning

I. INTRODUCTION

X-RAY computed tomography (CT) is an essential biomedical imaging technique for visualizing the anatomy of observed objects. CT reconstruction aims to solve the spatial distribution of linear attenuation coefficients (LACs) of the objects to X-rays. The LACs of the biological tissue remain nearly constant over X-ray spectra, while those of metals exhibit significant variations. This physical discrepancy causes a non-negligible nonlinear beam hardening effect (BHE) in CT measurements when the objects contain metals [1]. Hence, recovering the LAC map from metal-affected measurements poses a complicated nonlinear inverse problem. Traditional linear algorithms, such as filtered back-projection (FBP) [2], often cause severe artifacts in the CT images. These artifacts could significantly reduce the reliability of clinical diagnosis and biomedical research, such as bone analysis.

As an essential and longstanding issue in CT imaging, many efforts have been made to tackle metal artifacts reduction (MAR) [3]. Model-based [4]–[6] methods formulate the MAR as an image inpainting problem. They consider metal-corrupted signals in the raw measurements as missing data and design different schemes (*e.g.*, linear interpolation) to fill in these missing data. However, such paradigms typically cause apparent secondary artifacts in the reconstructions since the interpolation algorithms cannot meet the geometry constraints of CT scanning. Recently, supervised deep learning (DL) approaches [7]–[13] dominate the MAR task, in which deep neural networks normally are trained for learning mappings from the metal-affected measurements to clear measurements or the artifacts-corrupted images to the desired high-quality images. Benefiting from powerful neural networks and data-driven priors, supervised DL methods produce state-of-the-art (SOTA) MAR performance. However, they still face two major limitations: 1) A large-scale training dataset comprising numerous paired samples is required for supervised learning. However, collecting such paired datasets is a very challenging task; 2) Supervised learning often suffers from performance drops when CT acquisition protocols (*e.g.*, differences in metal shapes and X-ray acquisition geometry) deviate from those in the training dataset, *i.e.*, out-of-domain (OOD) problem. The two limitations considerably hamper the practical use of the supervised MAR models in real-world scenarios.

This work was supported by the National Natural Science Foundation of China under Grants No. 62071299 (*Corresponding author: Yuyao Zhang*).

Qing Wu is with the School of Information Science and Technology, ShanghaiTech University, Shanghai 201210, China, and with the Shanghai Advanced Research Institute, Chinese Academy of Sciences, Shanghai 201210, China, and also with the University of Chinese Academy of Sciences, Beijing 101408, China (e-mail: wuqing@shanghaitech.edu.cn).

Xu Guo and Yifeng Zhang are with the School of Life Science and Technology, ShanghaiTech University, Shanghai 201210, China (e-mail: guoxu@shanghaitech.edu.cn; zhangyf3@shanghaitech.edu.cn).

Lixuan Chen is with the School of Information Science and Technology, ShanghaiTech University, Shanghai 201210, China (e-mail: chenlx1@shanghaitech.edu.cn).

Dongming He and Xudong Wang are with Shanghai Ninth People's Hospital, Shanghai Jiao Tong University School of Medicine, Shanghai, China (e-mail: 1295227946@qq.com; xudongwang70@hotmail.com)

Hongjiang Wei is with the School of Biomedical Engineering, Shanghai Jiao Tong University, 200127 Shanghai, China (e-mail: hongjiang.wei@sjtu.edu.cn).

S. Kevin Zhou is with the School of Biomedical Engineering & Suzhou Institute for Advanced Research, Center for Medical Imaging, Robotics, Analytic Computing & Learning (MIRACLE), University of Science and Technology of China, Suzhou, CN (e-mail: skevinzhou@ustc.edu.cn).

Jingyi Yu and Yuyao Zhang are with the School of Information Science and Technology and Shanghai Engineering Research Center of Intelligent Vision and Imaging, ShanghaiTech University, Shanghai 201210, China (e-mail: yujingyi@shanghaitech.edu.cn; zhangyy8@shanghaitech.edu.cn).

Implicit neural representation (INR) has recently emerged as an innovative unsupervised framework for addressing inverse problems in image reconstruction. It first represents an unknown image as an implicit function that maps spatial coordinates into image pixels. Through the integration of differentiable physical forward models (*e.g.*, Fourier transform for MRI and Radon transform for parallel CT), the unknown image can be transformed into the measurement domain (*e.g.*, K-space data for MRI and projection data for CT). Using a multi-layer perception (MLP) to approximate the implicit function allows the unknown image to be solved by minimizing predicted errors between the estimated and real measurements. The unsupervised learning makes the INR great practical for numerous reconstruction problems. Moreover, the MLP networks induce an inherent learning bias towards low-frequency signals [14], [15]. This bias can be viewed as an implicit regularization prior, enabling the INR to provide a stable and feasible solution for under-determined inverse problems. By simplifying the CT forward acquisition as a linear integral (*i.e.*, Radon transformation), the INR has demonstrated great potential for various CT reconstruction tasks (*e.g.*, sparse-view CT [16]–[22], limited-angle CT [20], [22], and dynamic CT [23]–[25]). However, existing INR-based methods fail to handle the nonlinear MAR problem since the current linear integral model supposes that LACs are monochromatic strictly (*i.e.*, energy-independent), which leads to the nonlinear BHE being ignored.

In this paper, we propose a novel unsupervised density neural representation (Diner) to tackle the MAR problem from a nonlinear perspective. Our Diner proposes to introduce an energy-dependent polychromatic CT forward model (Eq. (3)) to the INR framework, enabling its capacity to address the nonlinear nature of the MAR problem. Specifically, by fully considering the physical model of X-ray absorption, we disentangle the energy-dependent LAC map into two essential components: an energy-independent density map and an energy-dependent mass attenuation coefficient (MAC) map. Using the MAC map as known prior knowledge, we then use the INR network to solve the unknown density map. Therefore, the polychromatic LAC maps at different X-ray energy levels can be accurately generated by performing the polychromatic CT forward model on the estimated density map. As reliable predictions for polychromatic LAC maps can be achieved, our Diner fundamentally addresses the energy-induced nonlinear BHE and thus facilitates effective MAR reconstructions.

Technically, we represent the unknown density map as an implicit function of spatial coordinates. Then, we optimize an MLP network to learn the function from the metal-affected measurements. We make two key technical contributions to perform the challenging nonlinear optimization problem. Firstly, we propose a novel differentiable physical forward model that can accurately simulate the acquisition process from the underlying densities to the measurements. Secondly, we incorporate the proposed forward model with the INR framework, enabling its capacity to solve the nonlinear inverse problem. Our Diner is a fully unsupervised technique and thus does not require any external training data, improving its great potential for a variety of clinical applications. We evaluate the proposed Diner model on four datasets, including

two simulated datasets and two real-world datasets. Empirical results demonstrate that our unsupervised Diner performs slightly better than well-known supervised MAR techniques on in-domain datasets while significantly outperforming them on out-of-domain datasets.

The main contributions of this work are as follows:

- We propose Diner, an unsupervised physical-model-driven DL approach, that can recover high-quality CT images from metal-corrupted measurements without involving external training data.
- We propose a novel formulation for the nonlinear MAR problem, that is, solving the energy-independent density map, which fundamentally addresses the energy-induced nonlinear BHE.
- We propose a novel differentiable forward model that can accurately simulate the physical acquisition process from the underlying densities to the CT measurements.
- We incorporate the proposed forward model into the INR framework, enabling its capacity to handle the nonlinear MAR inverse problems.

This study follows our previous study Polyner [26] and performs several substantial improvements. Polyner [26] tackles the MAR problem by directly representing the polychromatic LAC maps at multiple energy levels using the INR framework. This significantly alleviates the energy-induced BHE. However, the prediction of numerous (# of multiple energy levels) LAC maps poses a severely ill-posed under-determined inverse problem. In Polyner [26], the solution is merely constrained by an extra local smooth regularization. Compared with Diner, Polyner [26] has a significantly higher number of unknown variables, and the regularization is not sufficiently robust. Consequently, this inadequacy makes it challenging to ensure a reliable prediction of the polychromatic LAC maps. In comparison, Diner proposes a novel strategy to unravel the energy-dependent LAC map by utilizing the density map and MAC map. This approach reduces the number of unknown variables to a single-density map, substantially reducing the under-determination level. A better MAR reconstruction thus can be yielded. Moreover, this work conducts a more comprehensive experimental evaluation (including multiple types of simulated metal materials, real-world 3D cone-beam mouse data, real-world 3D helical phantom data following clinical CT acquisition protocol, extensive ablation studies, failure cases, etc.), which significantly strengthens the reliability of the proposed method.

II. PRELIMINARIES

The Lambert-Beer’s law [27], [28] formulates the physical process of an X-ray passing through an object as below:

$$I(\mathbf{r}, E) = I_0(E_0) \cdot \exp\left(-\int_{\mathbf{r}} \mu(\mathbf{x}, E_0) d\mathbf{x}\right), \quad (1)$$

where \mathbf{r} represents a monochromatic (*i.e.*, single-energy) X-ray, E_0 is its energy level, $I_0(E)$ and $I(\mathbf{r}, E)$ respectively are the numbers of photons emitted by an X-ray source and received by an X-ray detector, and $\mu(\mathbf{x}, E)$ is the LAC of the object at the position \mathbf{x} . The LAC value serves as a measure of the capacity of the object to absorb the X-ray.

The CT measurements $p(\mathbf{r})$ are typically defined as a linear integral of the LACs μ along the X-ray \mathbf{r} :

$$p(\mathbf{r}) \triangleq -\ln \frac{I(\mathbf{r}, E_0)}{I_0(E_0)} = \int_{\mathbf{r}} \mu(\mathbf{x}, E_0) d\mathbf{x}. \quad (2)$$

The CT reconstruction problem is to solve the spatial distribution of the LACs $\mu(\mathbf{x}, E_0)$ from the measurement data p . When the Nyquist-Shannon sampling theorem is satisfied [29], standard techniques (*e.g.*, FBP [2]) for linear inverse problems can produce high-quality CT images.

However, most clinical CT scanners emit polychromatic X-rays (*i.e.*, within a range of energy levels) due to physical limitations of the X-ray generator hardware [1]. Given an X-ray composed of multiple monochromatic X-rays within a range of \mathcal{E} , the CT measurement data can be expressed by a nonlinear polychromatic model:

$$\begin{aligned} p(\mathbf{r}) &= -\ln \frac{\int_{\mathcal{E}} I(\mathbf{r}, E) dE}{\int_{\mathcal{E}} I_0(E) dE} \\ &= -\ln \int_{\mathcal{E}} \eta(E) \cdot \exp\left(-\int_{\mathbf{r}} \mu(\mathbf{x}, E) d\mathbf{x}\right) dE, \end{aligned} \quad (3)$$

where $\eta(E) = I_0(E) / \int_{\mathcal{E}} I_0(E') dE'$ represents the normalized energy spectrum that characterizes the distribution of the number of photons $I_0(E)$ emitted by the X-ray source over the energy level E .

The LACs of the biological tissue almost remain constant with increasing the energy level of the X-ray [7], [8], [11]. A common assumption for the biological tissue is:

$$|\mu(\mathbf{x}, E_a) - \mu(\mathbf{x}, E_b)| \approx 0, \quad \forall E_a, E_b \in \mathcal{E}, \quad (4)$$

i.e., the LACs of the biological tissue are considered energy-independent. Thus, we can represent their LACs as a function of spatial coordinates $\mu(\mathbf{x})$ and then derive the corresponding measurement data as below:

$$p(\mathbf{r}) = -\ln \int_{\mathcal{E}} \eta(E) \cdot \exp\left(-\int_{\mathbf{r}} \mu(\mathbf{x}) d\mathbf{x}\right) dE = \int_{\mathbf{r}} \mu(\mathbf{x}) d\mathbf{x}. \quad (5)$$

This implies that the CT acquisition for the biological tissue can still be approximated as a linear integral transformation when even using polychromatic X-rays. Therefore, the CT images by FBP [2] are artifacts-free in this case.

However, the LACs of metallic materials undergo sharp variations as a function of the energy spectrum of the X-rays [1]. For an organism with metallic implants, we thus have to split its LAC map into two parts: tissue region and metal region. Mathematically, it can be expressed as:

$$\mu(\mathbf{x}, E) = [1 - \mathcal{M}(\mathbf{x})] \cdot \mu_{\text{tissue}}(\mathbf{x}) + \mathcal{M}(\mathbf{x}) \cdot \mu_{\text{metal}}(\mathbf{x}, E), \quad (6)$$

where $\mu_{\text{tissue}}(\mathbf{x})$ and $\mu_{\text{metal}}(\mathbf{x}, E)$ denote the LACs of the tissue and metal, respectively. \mathcal{M} is a metal binary mask ($\mathcal{M} = 1$ for the metal region and $\mathcal{M} = 0$ otherwise).

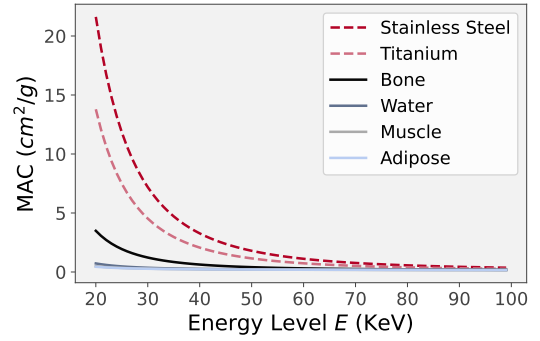


Fig. 1. MAC curves of different materials over the X-ray energy range E of [20, 100] KeV. The data is from the XCOM database [30].

Substituting Eq. (6) into Eq. (3), the CT measurement data can be derived as below:

$$\begin{aligned} p(\mathbf{r}) &= \underbrace{\int_{\mathbf{r}} [1 - \mathcal{M}(\mathbf{x})] \cdot \mu_{\text{tissue}}(\mathbf{x}) d\mathbf{x}}_{\text{Linear Integral}} \\ &\quad - \underbrace{\ln \int_{\mathcal{E}} \eta(E) \cdot \exp\left(-\int_{\mathbf{r}} \mathcal{M}(\mathbf{x}) \cdot \mu_{\text{metal}}(\mathbf{x}, E) d\mathbf{x}\right) dE}_{\text{Nonlinear Beam Hardening Effect}}. \end{aligned} \quad (7)$$

Eq. (7) means that the CT measurements of an organism with metallic implants should be divided into two parts: (1) a linear integral for the tissue and (2) an energy-induced non-linear transformation for the metals. The latter is known as the nonlinear beam hardening effect (BHE) in the CT measurements. In this case, the use of traditional linear algorithms, such as FBP [2], will result in severe metal artifacts in the resulting CT images.

III. METHODOLOGY

A. Problem Formulation

As illustrated in Eq. (7), the nonlinear BHE is the key factor for addressing the CT MAR problem. Previous MAR approaches [4], [5], [7], [31], [32] mostly assume that the LACs to be resolved are energy-independent and reconstruct them at a virtual monochromatic energy level. However, this paradigm fails to consider the energy-induced BHE, which results in the sub-optimal MAR performance.

In this work, we propose to directly reconstruct the densities of observed objects. The densities are physically energy-independent, which can fundamentally address the energy-induced BHE and thus significantly improve the MAR performance. As shown in Eq. (3), the CT measurement data p , however, is the nonlinear transform of the energy-dependent LACs μ . It is not directly related to the densities. To establish an explicit relationship between the measurement data p and densities, we innovatively introduce a standard physical model [33], [34] to decompose the LACs μ as a product of the densities σ and energy-dependent mass attenuation coefficients (MACs) γ , which is expressed as below:

$$\mu(\mathbf{x}, E) = \gamma(\mathbf{x}, E) \cdot \sigma(\mathbf{x}). \quad (8)$$

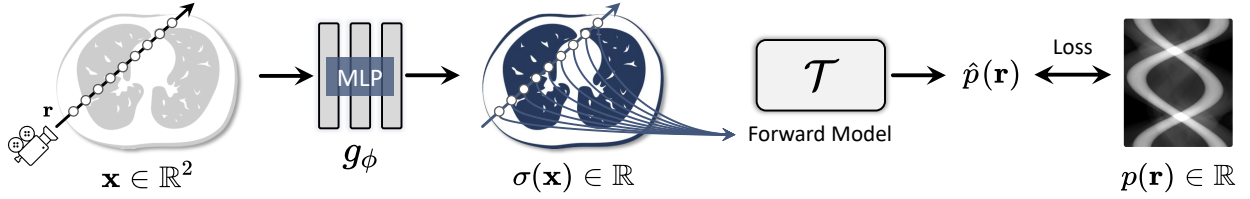


Fig. 2. Overview of the proposed Diner model. For an X-ray \mathbf{r} , we first sample a set of coordinates \mathbf{x} at a fixed interval $\Delta\mathbf{x}$. Then, we feed these coordinates \mathbf{x} into an MLP network g_ϕ to predict the densities $\sigma(\mathbf{x})$ of the observed object at these positions. Furthermore, we use the proposed nonlinear forward model \mathcal{T} (Eq. (12)) to transform these MLP-predicted densities $\sigma(\mathbf{x}), \forall \mathbf{x} \in \mathbf{r}$ into measurement data $\hat{p}(\mathbf{r})$. Finally, we minimize the predicted errors \mathcal{L}_{DC} between the estimated $\hat{p}(\mathbf{r})$ and raw $p(\mathbf{r})$ measurements to optimize the trainable weights of the MLP network g_ϕ for learning the density neural representation.

For organisms with metallic implants, we then make two basic assumptions:

Assumption 1. *The MACs of the biological tissue can be approximated by those of water, i.e., $\gamma(\mathbf{x}, E) \triangleq \gamma_{\text{water}}(E), \forall \mathbf{x} \notin \mathcal{M}$, where \mathcal{M} denotes metal regions.*

Assumption 2. *The metallic implants are homogeneous such that $|\gamma(\mathbf{x}_a, E) - \gamma(\mathbf{x}_b, E)| \approx 0, \forall \mathbf{x}_a, \mathbf{x}_b \in \mathcal{M}$ holds, and their position-independent MACs are accessible.*

Remark 1. *Experimental findings [35], [36] have shown that most types of biological tissue (e.g., adipose tissue and muscle tissue) have similar MACs that are very close to those of water. Figure 1 shows the MAC curves of two metals (titanium and 304 stainless steel), three types of human tissue (muscle, bone, and adipose), and water over the X-ray energy range of [20, 100] KeV. We observe that the three human tissues are significantly closer to water than the two metals.*

Remark 2. *Most common biomedical metallic implants (e.g., titanium and 304 stainless steel) are homogeneous, and their corresponding MACs can be easily accessible in some well-known open-source databases, such as NIST standard library [37] and XCOM program [30].*

According to assumptions 1 and 2, by substituting Eq. (8) into Eq. (6), we define a novel LACs decomposition model for the MAR task as below:

$$\mu(\mathbf{x}, E) = \sigma(\mathbf{x}) \cdot \left\{ [1 - \mathcal{M}(\mathbf{x})] \cdot \gamma_{\text{water}}(E) + \mathcal{M}(\mathbf{x}) \cdot \gamma_{\text{metal}}(E) \right\}, \quad (9)$$

where γ_{water} and γ_{metal} respectively denote the known MACs of the water and metals. Eq. (9) implies that the energy-dependent LACs $\mu(\mathbf{x}, E)$ can be reconstructed accurately by solving the energy-independent densities $\sigma(\mathbf{x})$. Hence, the CT MAR problem is formulated as a reconstruction problem of the densities of the observed objects.

B. Density Neural Representation

Figure 2 shows the workflow of solving the densities via the proposed Diner model. In this section, we introduce the main technical contributions of our Diner in detail.

1) *MLP-based Parameterization:* Without loss of generality, we present here our Diner model based on a 2D CT acquisition system for simplicity. However, the proposed approach can be easily extended to more advanced CT protocols (e.g., 3D cone-beam and helical CT) through a flexible geometry

implementation. Given a 2D CT acquisition system, we represent the density map to be reconstructed as a function of spatial coordinates, defined by

$$f : \mathbf{x} = (x, y) \in \mathbb{R}^2 \rightarrow \sigma \in \mathbb{R}, \quad (10)$$

where \mathbf{x} is any spatial coordinate and σ is the density of the object at the position \mathbf{x} . However, solving the analytical expression of the implicit function f is intractable.

Inspired by the recent advancements of the INR framework [38]–[41] for recovering signals, we employ an MLP network g_ϕ that takes a single coordinate \mathbf{x} and outputs the corresponding density σ to approximate the function (i.e., $f \approx g_\phi$). Technically, we optimize the trainable weights ϕ of the MLP network. Once the optimization is completed, the desired density map is parameterized into the weights ϕ . Taking advantage of the MLP network’s powerful fitting capability and learning bias for low-frequency signals [14], [15], such MLP-based parameterization can yield high-quality reconstructions in line with natural image manifolds.

2) *Differentiable Forward Model:* The output of the MLP network g_ϕ is expected as the density σ , a physical property of the observed object. We thus need to define a new physical forward model \mathcal{T} to simulate the complex acquisition process from the underlying property (i.e., density) to the raw CT measurements. Our forward model includes two stages:

- Performing our LACs decomposition model (Eq. (9)) to transform the MLP-predicted, energy-independent densities $\sigma(\mathbf{x}) = g_\phi(\mathbf{x})$ into the polychromatic LACs $\mu(\mathbf{x}, E)$ at multiple energy levels;
- Using the discrete version of the polychromatic model (Eq. (3)) to generate the estimated measurement $\hat{p}(\mathbf{r})$ from the polychromatic LACs $\mu(\mathbf{x}, E)$.

Formally, the discrete polychromatic model is defined as:

$$\hat{p}(\mathbf{r}) = -\ln \sum_{i=1}^N \eta(E_i) \cdot \exp \left(-\sum_{\mathbf{x} \in \mathbf{r}} \mu(\mathbf{x}, E_i) \cdot \Delta\mathbf{x} \right), \quad (11)$$

where $\Delta\mathbf{x}$ denotes the Euclidean distance between adjacent sampling coordinates along the X-ray \mathbf{r} . The normalized energy spectrum $\eta \in \mathbb{R}^N$ is considered a known prior knowledge. We use the SPEKTR toolkit [42] to estimate it. Its effects on the MAR reconstruction performance are explored in the following experiments.

In summary, our full forward model \mathcal{T} is defined by:

$$\mathcal{T} : \sigma(\mathbf{x}) \xrightarrow{\text{Eq. (9)}} \mu(\mathbf{x}, E) \xrightarrow{\text{Eq. (11)}} \hat{p}(\mathbf{r}). \quad (12)$$

TABLE I
DETAILED PARAMETERS OF THE ACQUISITION PROCESSES FOR THE DEEPLESION [43] AND LIDC [44] SIMULATION DATASETS AND MOUSE TIGHT AND BODY PHANTOM REAL-WORLD DATASETS.

| Parameters | Simulation Data | | Real-world Data | |
|--------------------|---------------------|-----------------------------------|----------------------------------|--|
| | DeepLesion/LIDC | Mouse Tight | Body Phantom | |
| Manufacturer | – | Bruker | UIH | |
| Geometry | Fan-beam | Cone-beam | Helical CT | |
| Image Size | 256×256 | 500×500×500 | 512×512×490 | |
| Voxel Size | 1×1 mm ² | 0.03 ³ mm ³ | 0.5 ³ mm ³ | |
| Source Voltage | – | 60 kV | 120 kV | |
| Scanning Range | [0, 360]° | [0, 360]° | [0, 360]° | |
| Angular Spacing | 0.1° | – | – | |
| Detector Spacing | – | 0.07 mm | 0.5 mm | |
| Source to Center | 362 mm | 92.60 mm | 570 mm | |
| Center to Detector | 362 mm | 65.95 mm | 490 mm | |
| Number of Angles | 360/270 | 900 | 48,867 | |

It is worth noting that this forward model \mathcal{T} is differentiable, enabling the use of gradient backpropagation algorithms to optimize the MLP network g_ϕ .

3) *Loss Function*: By leveraging the forward model \mathcal{T} , the MLP-predicted densities $\sigma(\mathbf{x}) = g_\phi(\mathbf{x}), \forall \mathbf{x} \in \mathbf{r}$ are transformed into the CT measurement data $\hat{p}(\mathbf{r})$. Then, we define a loss function \mathcal{L}_{DC} to compute the mean absolute error between the estimated \hat{p} and real measurements p . The loss function can provide data consistency with the real measurements p . It can be expressed as below:

$$\mathcal{L}_{DC} = \frac{1}{|\mathcal{R}|} \sum_{\mathbf{r} \in \mathcal{R}} |\hat{p}(\mathbf{r}) - p(\mathbf{r})|, \quad (13)$$

where \mathcal{R} denotes a set of randomly sampling X-rays \mathbf{r} at each training iteration.

C. Virtual Monochromatic CT Image Reconstruction

After the optimization, we feed all spatial coordinates \mathbf{x} into the well-trained MLP network to produce the corresponding densities $\sigma(\mathbf{x}) = g_\phi(\mathbf{x})$, meaning a density map $\sigma(\cdot)$ can be reconstructed. Then, we use our LACs decomposition model (Eq. (9)) to generate the energy-dependent LAC maps $\mu(\cdot, E)$ at N energy levels (*i.e.*, polychromatic CT images). However, this work aims to recover a single monochromatic artifact-free CT image. Consider a polychromatic X-ray composed of multiple monochromatic X-rays at N energy levels, the energy level of its equivalent monochromatic X-ray is given by:

$$E^* = \left\lfloor \sum_{i=1}^N \eta(E_i) \cdot E_i \right\rfloor, \quad (14)$$

where $\lfloor \cdot \rfloor$ represents floor function. Finally, the LAC map $\mu(\cdot, E^*)$ at the energy level E^* is employed for the artifact-free reconstruction output.

D. Implementation Details

For our Diner, we employ the recent hash encoding [41] followed by two fully connected (FC) layers to implement the MLP network g_ϕ . The hash encoding can effectively accelerate the training process. Its hyper-parameters are set as below: $L = 16$, $T = 2^{19}$, $F = 8$, $N_{\min} = 2$ and $b = 2$. The two

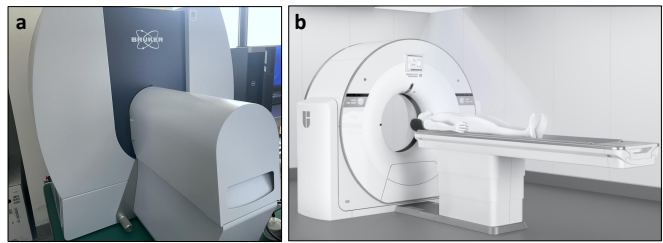


Fig. 3. (a) The commercial Bruker SKYSCAN 1276 micro-CT scanner used in our mouse tight data acquisition and (b) The commercial UIH uCT 768 scanner used in our body phantom data acquisition.

FC layers have 128 neurons, followed by ReLU and ELU activation functions, respectively. At each training iteration, we set the number of the random sampling X-rays as 80, *i.e.*, $|\mathcal{R}| = 80$ in Eq. (13). We use the Adam optimizer [45] with default hyperparameters. The learning rate starts from $1e-3$ and decays by half per 500 epochs. The total training epochs is 2000, which takes about 1.2 minutes on a single NVIDIA RTX TITIAN GPU. Note that all hyper-parameters are tuned on 10 samples from the DeepLesion dataset [43] and then fixed across all other samples.

IV. EXPERIMENTS

We conduct comprehensive experiments to assess the effectiveness of our proposed approach, including i) Comparison with the SOTA MAR methods on both simulated and real-world datasets, ii) Extensive ablation studies to analyze and understand the components and intricacies of our Diner, and iii) An examination of failure cases and limitations of our Diner. The empirical studies confirm the superiority of our unsupervised Diner over existing MAR methods in terms of MAR performance and robustness.

A. Data

We conduct experiments on four diverse datasets, including two simulation datasets and two real-world datasets. Table I shows the detailed parameters of the four datasets.

1) *DeepLesion and LIDC Simulation Datasets*: DeepLesion [43] and LIDC [44] are the two most commonly used datasets for the CT MAR evaluation. For the two datasets, we extract 50 and 20 two-dimensional (2D) slices, respectively, from raw three-dimensional (3D) CT volumes as ground truth (GT) samples. Then, we follow the data pre-processing pipeline presented in the prior studies [7], [8], [11] to synthesize metal-corrupted measurements as input data. Specifically, we use ten shapes of metals provided by Zhang *et al.* [7] and simulate three types of common medical materials (including titanium, chromium, and 304 stainless steel) according to the XCOM database [30]. We simulate a polychromatic X-ray source by following literature [7], [9]–[11]. We also incorporate Poisson noise and the partial volume effect into the measurement data. Table I shows the detailed parameters of the acquisition processes for the two simulation datasets. It is worth noting that all data are solely used for the test since our method is fully unsupervised.

TABLE II

QUANTITATIVE RESULTS OF COMPARED METHODS FOR THREE TYPES OF METALS ON THE DEEPLesion [43] AND LIDC [44] SIMULATION DATASETS. THE BEST AND SECOND PERFORMANCES ARE RESPECTIVELY HIGHLIGHTED IN **BOLD** AND UNDERLINE. THE SUBSCRIPTS ♣, ♠, ◇, AND ♣ RESPECTIVELY REPRESENT MODEL-BASED, UNPAIRED-SUPERVISED, SUPERVISED, AND UNSUPERVISED MAR TECHNIQUES.

| Dataset | Method | Types of Metals | | | | | |
|-----------------|---------------|-------------------|----------------------|-------------------|----------------------|---------------------|----------------------|
| | | TITANIUM | | CHROMIUM | | 304 STAINLESS STEEL | |
| | | PSNR | SSIM | PSNR | SSIM | PSNR | SSIM |
| DeepLesion [43] | FBP♣ [2] | 30.61±2.71 | 0.7829±0.0804 | 26.67±2.89 | 0.6465±0.1052 | 25.01±2.95 | 0.5888±0.1098 |
| | LI♣ [4] | 32.07±2.61 | 0.8650±0.0518 | 32.07±2.61 | 0.8650±0.0518 | 32.07±2.61 | 0.8650±0.0518 |
| | ART♣ [6] | 32.60±3.02 | 0.8502±0.0554 | 32.60±3.02 | 0.8502±0.0554 | 32.60±3.02 | 0.8502±0.0554 |
| | ADN♠ [11] | 33.83±2.48 | 0.9508±0.0156 | 32.58±3.16 | 0.9409±0.0223 | 31.77±3.54 | 0.9340±0.0263 |
| | CNN-MAR◇ [7] | 35.05±2.31 | 0.9385±0.0218 | 34.71±2.38 | 0.9322±0.0257 | 34.50±2.44 | 0.9277±0.0289 |
| | DICDNet◇ [10] | 37.93±1.89 | 0.9710±0.0094 | 37.18±2.21 | 0.9654±0.0128 | 36.74±2.47 | 0.9623±0.0148 |
| | ACDNet◇ [9] | <u>38.43±1.91</u> | 0.9701±0.0112 | <u>37.46±2.25</u> | 0.9586±0.0171 | <u>36.90±2.50</u> | 0.9524±0.0200 |
| | Polyner♣ [26] | 37.23±1.62 | 0.9769±0.0048 | 36.96±2.00 | 0.9754±0.0057 | 36.65±2.48 | 0.9739±0.0069 |
| | Diner♣ (Ours) | 39.17±1.85 | 0.9846±0.0035 | 38.77±1.81 | 0.9824±0.0043 | 38.57±1.78 | 0.9814±0.0048 |
| | LIDC [44] | FBP♣ [2] | 25.87±2.23 | 0.5435±0.1219 | 22.20±2.43 | 0.4063±0.1201 | 20.63±2.54 |
| LI♣ [4] | | 29.30±2.38 | 0.7457±0.0941 | 29.30±2.38 | 0.7457±0.0941 | 29.30±2.38 | 0.7457±0.0941 |
| ART♣ [6] | | 27.99±2.97 | 0.6565±0.1069 | 27.99±2.97 | 0.6565±0.1069 | 27.99±2.97 | 0.6565±0.1069 |
| ADN♠ [11] | | 22.01±3.84 | 0.8220±0.0687 | 21.61±3.69 | 0.7866±0.0760 | 21.29±3.67 | 0.7669±0.0826 |
| CNN-MAR◇ [7] | | 30.53±1.93 | 0.8148±0.0738 | 30.26±2.18 | 0.8017±0.0848 | 30.13±2.27 | 0.7956±0.0902 |
| DICDNet◇ [10] | | 30.16±2.80 | 0.9239±0.0357 | 28.75±3.40 | 0.9061±0.0447 | 28.10±3.67 | 0.8948±0.0510 |
| ACDNet◇ [9] | | 29.98±3.12 | 0.9259±0.0420 | 27.57±4.38 | 0.9045±0.0608 | 26.84±4.65 | 0.8947±0.0671 |
| Polyner♣ [26] | | <u>31.62±2.49</u> | 0.9497±0.0265 | 31.75±2.08 | <u>0.9462±0.0267</u> | 31.37±2.28 | 0.9450±0.0284 |
| Diner♣ (Ours) | | 33.75±1.12 | 0.9514±0.0243 | 33.53±1.16 | 0.9487±0.0247 | 33.43±1.17 | 0.9472±0.0254 |

2) *Mouse Tigh Real-world Dataset*: To evaluate the effectiveness of our Diner model in biomedical X-ray CT settings, we scan five mouse-thigh samples containing intramedullary needles of 304 stainless steel metal on a commercial Bruker SKYSCAN 1276 micro-CT scanner, as shown in Figure 3. The CT acquisition protocol is shown in Table I. We use the SPEKIT toolkit [42] to estimate the X-ray energy spectrum of the scanner. The Ethics Committee of ShanghaiTech University approves this data collection.

3) *Body Phantom Real-world Dataset*: To test the MAR performance of the proposed method on clinical helical CT, we measure a human body phantom containing Ti metals using a commercial UIH X-ray CT scanner (uCT 768). To align with clinical settings, we use a standard clinical acquisition protocol, which is demonstrated in Table I. This data acquisition is approved by UIH Co., Ltd. and the Ethics Committee of ShanghaiTech University.

B. Baselines and Evaluation Metrics

We compare the proposed Diner with eight representative MAR methods belonging to four categories: i) Three model-based methods (FBP [2], LI [4], and ART [6]); ii) Three supervised DL methods (CNN-MAR [7], DICDNet [10], and ACDNet [9]); iii) One unpaired-supervised DL method (ADN [11]); iv) One unsupervised DL method (Polyner [26]). It should be noted that the supervised and unpaired-supervised DL methods are evaluated based on the pre-trained models provided by the authors to ensure a fair comparison. Among them, CNN-MAR [7] is trained on the XCOM dataset [30],

while DICDNet [10], ACDNet [9], and ADN [11] are trained on the DeepLesion dataset [43].

We use peak signal-to-noise ratio (PSNR) and structural similarity index measure (SSIM) [46] as quantitative metrics and implement them by the Python library scikit-image [47].

C. Comparison with Baselines on Simulation Data

Table II shows the quantitative results. Generally, our Diner produces the best performance for all cases. On the DeepLesion dataset [43], our unsupervised Diner not only significantly outperforms the unsupervised Polyner [26], but also slightly performs better than the two supervised methods (DICDNet [10] and ACDNet [9]). For example, the PSNR respectively improves by +1.94 dB, +1.24 dB, and +0.74 dB for the titanium metals. While on the LIDC dataset [44], the supervised ACDNet and ACDNet trained on the DeepLesion dataset [43] fail to achieve pleasant MAR performance due to the OOD problem. They even perform worse than the traditional model-based LI algorithm [4], such as -2.46 dB and -1.20 dB in the PSNR for the 304 stainless steels. In comparison, our Diner still yields the best MAR reconstructions, outperforming the second-best Polyner [26] by about +2.06 dB in PSNR for the 304 stainless steels. We show the qualitative results in Figure 4. Traditional FBP algorithm [2] and supervised CNN-MAR trained on the XCOM [30] cannot recover satisfactory results, including severe artifacts on both datasets. While ACDNet produces a clear but slightly smooth MAR reconstruction on the DeepLesion dataset [43], its result on the LIDC dataset suffers from severe shadow artifacts. In comparison, the two unsupervised methods (Polyner [26] and our Diner) achieve

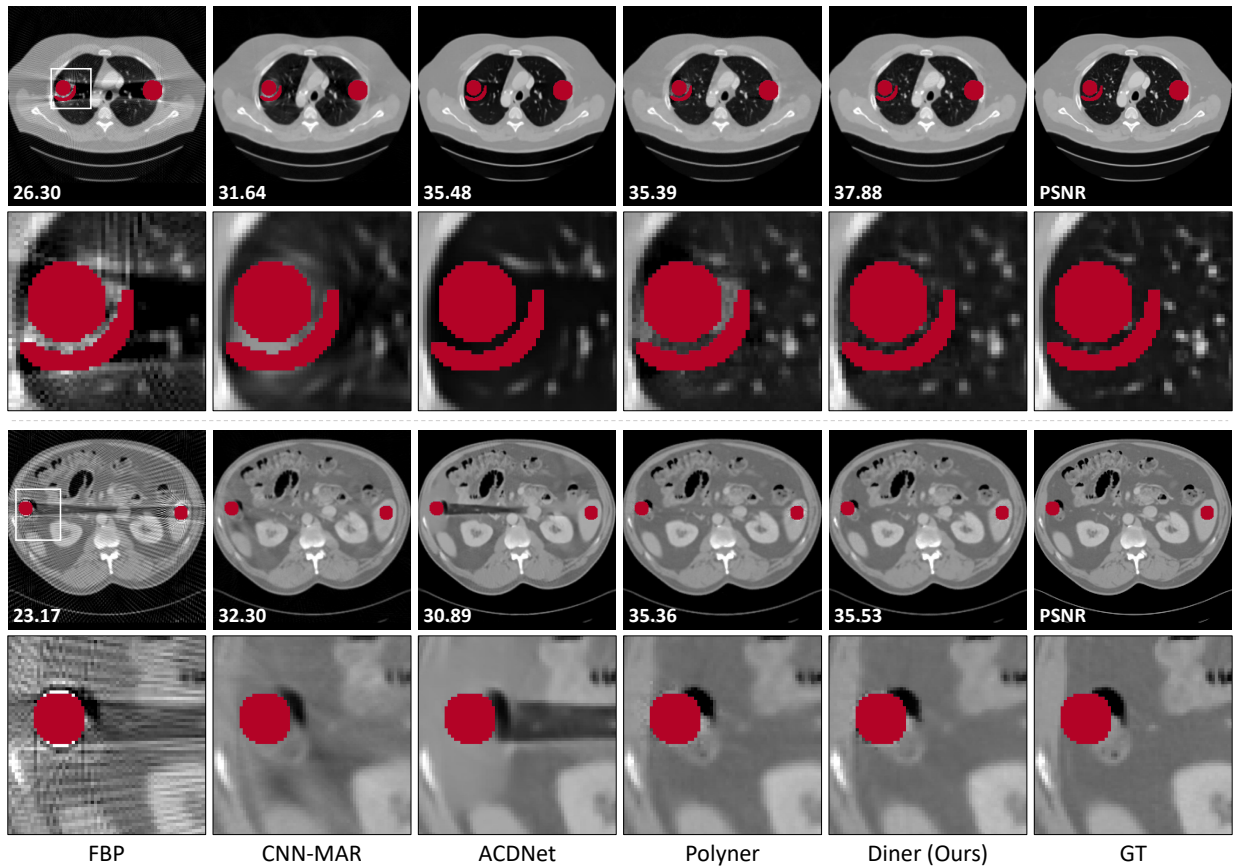


Fig. 4. Qualitative results of four compared methods and our Diner on two samples (#100 (top-two rows) and #50 (bottom-two rows)) of the DeepLesion [43] and LIDC [44] datasets. The red regions denote metals.

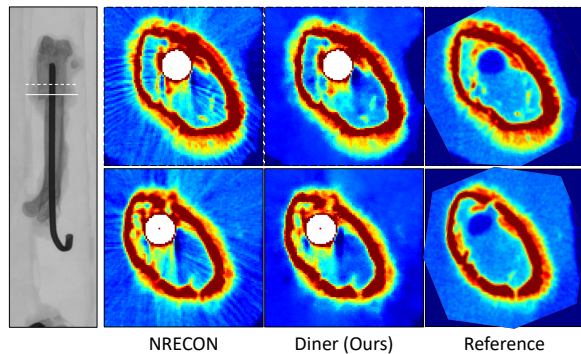


Fig. 5. (Left) A sample among 2D projections for a mouse-thigh sample containing an intramedullary needle. (Right) Qualitative results of NRECON (*i.e.*, a reconstruction toolkit developed by Bruker and equipped with Bruker SKYSCAN 1276 micro-CT scanner) and our Diner on the needle-corrupted measurement. The reference image is the clear version of the mouse thigh sample after removing the intramedullary needle. The white regions denote the intramedullary needle.

robust results across the two datasets. However, the results of Polyner [26] contain slight artifacts around the metal, while our Diner produces clean and fine-detailed MAR reconstruction.

D. Comparison with Baselines on Real-world Data

1) *On Mouse Thigh Dataset:* We collect five mouse-thigh samples containing an intramedullary needle with a commercial

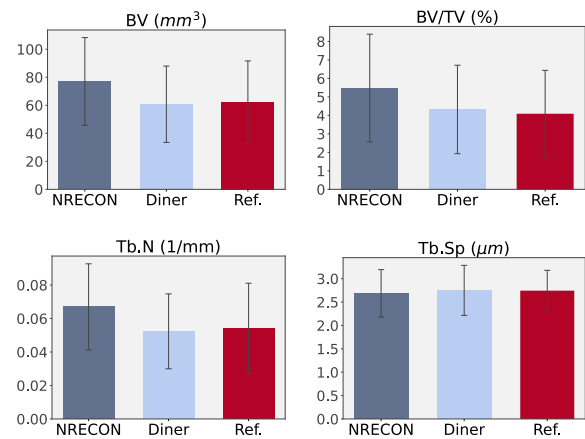


Fig. 6. Qualitative results of bone analysis on the CT volumes of the five mouse-thigh samples containing an intramedullary needle. Here BV, BV/TV, Tb.N, and Tb.SN respectively denotes bone volume, percent bone volume, trabecular number, and trabecular separation. NRECON is a reconstruction toolkit developed by Bruker and equipped with Bruker SKYSCAN 1276 micro-CT scanner. Ref. is produced by NRECON on the clear measurement.

Bruker SKYSCAN 1276 micro-CT scanner. The initial intent of the mouse model is to investigate the progress of bone-fracture healing in mice. The setup is shown in Figure 3. The intramedullary needle was implanted into the mouse thigh one week before the CT scan. To further assess the accuracy

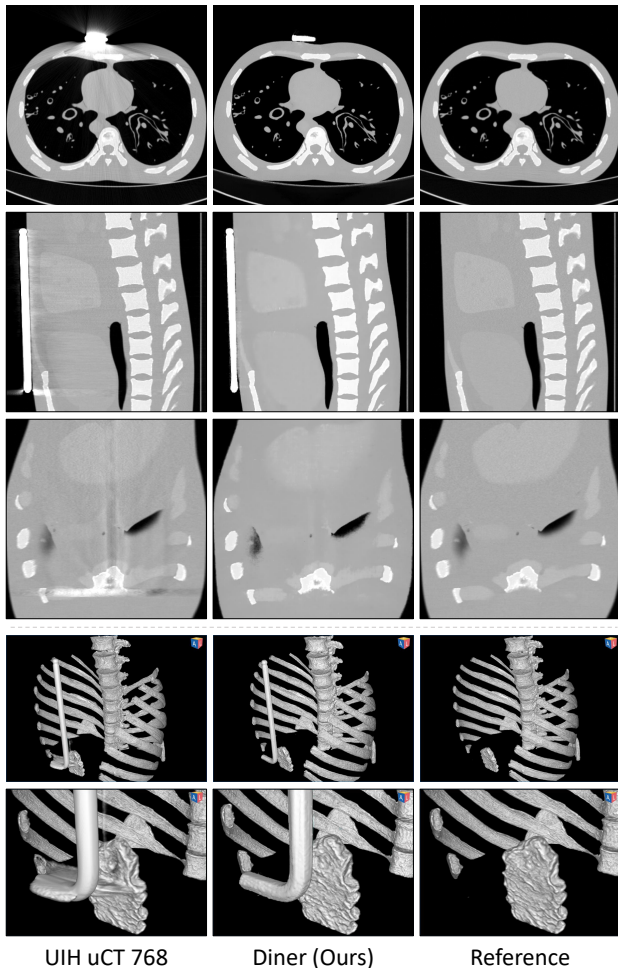


Fig. 7. (Rows 1–3) Qualitative results of the reconstruction algorithm equipped with the UIH uCT 768 scanner and our Diner on the metal-corrupted body phantom without the metal. (Rows 4–5) Volume rendering of the CT volumes by using the Bee DICOM Viewer software (<https://beedicom.com/>).

of MAR CT reconstruction, the mouse thighs are scanned twice before and after needle removal. The reference image is the clear version of the mouse thigh sample after removing the intramedullary needle. We show the qualitative results in Figure 5. Compared with NRECON, a reconstruction toolkit developed by Bruker and equipped with Bruker SKYSCAN 1276 micro-CT scanner, our Diner produces a clear CT reconstruction closer to reference. Moreover, we use CTan, a bone analysis software developed by Bruker, to perform a bone analysis on these CT volumes. The results are shown in Figure 6. In terms of bone volume (BV), percent bone volume (BV/TV), and trabecular number (Tb.N), the reconstruction of NRECON obtain distinct higher scores than the clear reference image. This is because the metal artifacts in the CT volume are identified as high-density bone tissue by the CTan software. In comparison, our Diner effectively removes these metal artifacts and thus obtains very close scores to the reference image.

2) *On Body Phantom Dataset:* We conduct scans on two versions (with and without a metal stick) of a body phantom using the UIH commercial uCT 768 scanner according

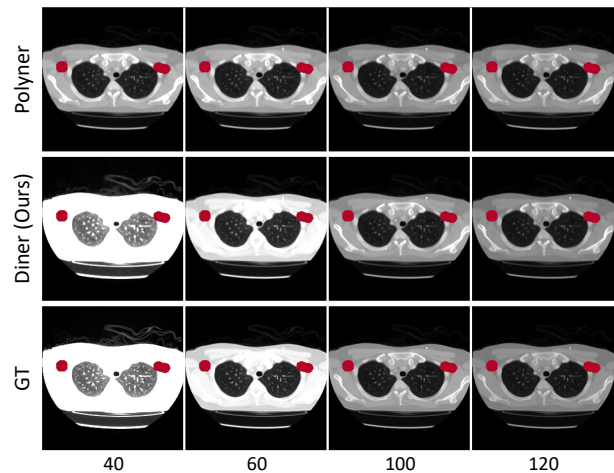


Fig. 8. Qualitative results of polychromatic images at four energy levels $E = \{40, 60, 100, 120\}$ by our Diner and Polyner [26] on a sample of the DeepLesion dataset [43]. The red regions denote metals.

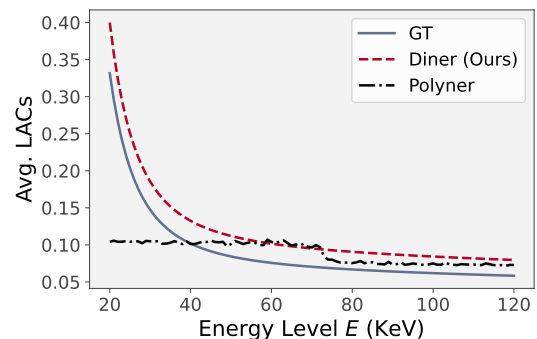


Fig. 9. Average LAC curves of polychromatic images by Polyner [26] and our Diner on a sample of the DeepLesion dataset [43] over the X-ray energy levels of [20, 120] KeV.

to a clinical acquisition protocol (See Table I for detailed parameters). The experimental setup is depicted in Figure 3. The qualitative results are presented in Figure 7. Here, “UIH uCT 768” denotes the reconstruction generated by the algorithm integrated into the clinical UIH uCT 768 scanner. Upon visual inspection of the CT slices from axial, sagittal, and coronal views (Rows 1–3), our Diner effectively reduces metal artifacts while finely preserving image details. Additionally, we utilize the Bee DICOM Viewer software for volume rendering of the CT reconstructions. These results are illustrated in Figure 7 (Rows 4–5). Also, the rendering outcome of our Diner is clear and fine-detailed, closely resembling that of the reference image. In summary, these ongoing experimental investigations conducted using the UHI uCT 768 scanner robustly demonstrate the efficacy of our Diner in clinical settings.

E. Reconstruction of Polychromatic Images

In our previous Polyner [26], the recovery of the polychromatic CT images is ill-posed on the spectrum distribution. In contrast, our Diner solves the energy-independent density map, which improves the reconstruction of the energy-dependent LACs. By conducting our LAC decomposition model (Eq. (9)),

TABLE III
QUANTITATIVE RESULTS OF POLYCHROMATIC CT IMAGES
RECONSTRUCTED BY OUR DINER AND POLYNNER [26] FOR THREE TYPES
OF METALS ON THE DEEPLesion DATASET [43].

| Method | Types of Metals | PSNR | SSIM |
|--------------|-----------------|-------------------|----------------------|
| Polyner [26] | TITANIUM | 29.75±5.16 | 0.9349±0.0738 |
| | CHROMIUM | 29.71±5.14 | 0.9336±0.0736 |
| | STAINLESS STEEL | 29.54±5.00 | 0.9320±0.0732 |
| Diner (Ours) | TITANIUM | 37.31±2.36 | 0.9820±0.0052 |
| | CHROMIUM | 37.05±2.28 | 0.9800±0.0056 |
| | STAINLESS STEEL | 36.92±2.24 | 0.9790±0.0059 |

TABLE IV
QUANTITATIVE RESULTS OF OUR DINER WITH DIFFERENT FORWARD
MODELS ON THE DEEPLesion DATASET [43].

| Forward Model | PSNR | SSIM |
|-------------------------------|-------------------|----------------------|
| Linear Integral | 34.47±2.47 | 0.9578±0.0137 |
| Nonlinear Model \mathcal{T} | 39.19±1.44 | 0.9844±0.0029 |

we can generate the LAC maps from the resolved density map. Here, we compare our Diner with Polyner for reconstructing the polychromatic images. Figure 8 show the solved polychromatic images at four energy levels $E = \{40, 60, 100, 120\}$. From the visualization, we observe that the results of our Diner model are very close to the GT samples in terms of image structure and contrast. In comparison, the reconstructions of Polyner are satisfactory for image structure but inconsistent for image contrast, *i.e.*, spectrum distribution. We show the average LAC curve of the polychromatic images over the X-ray energy in Figure 9. Polyner model produces an over-smooth spectrum distribution due to an energy-smooth regulation. In contrast, our Diner is highly consistent with GT, benefiting from the LAC decomposition model (Eq. (8)). Table III also shows the quantitative results of polychromatic images by Polyner [26] and Diner for all cases. The proposed Diner significantly improves the performance.

F. Ablation Studies

1) *Influence of Forward Model*: Our Diner proposes a new forward model \mathcal{T} (Eq. (12)) to enable the INR network to reconstruct the densities of the object. Here, we explore the influence of the forward model \mathcal{T} on the MAR performance. Specifically, we replace it with the linear integral model (Eq. (3)) used in the existing SOTA MAR techniques [2], [4], [7], [9]–[11] and make all other model configurations the same for a fair comparison. Table IV shows the quantitative results. Our proposed nonlinear model \mathcal{T} produces significant performance improvements compared with the conventional linear integral, where PSNR improves by +4.72 dB. We show the qualitative results in Figure 10. The linear model fails to tackle the shadow artifacts caused by the BHE. In comparison, the result of our nonlinear model is visually clear and very close to the GT sample. The experimental comparison indicates that our nonlinear model is critical for the MAR reconstructions.

2) *Influence of Energy Spectrum Prior*: In our forward model \mathcal{T} , the X-ray energy spectrum $\eta \in \mathbb{R}^N$ is considered

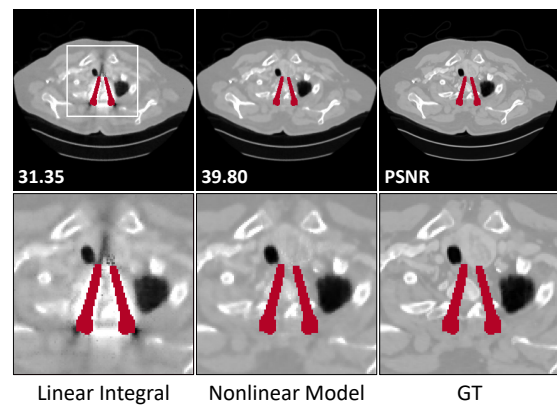


Fig. 10. Qualitative results of our Diner with different forward models on a sample of the DeepLesion dataset [43]. The red regions denote metals.

TABLE V
QUANTITATIVE RESULTS OF OUR DINER WITH DIFFERENT SPECTRUM
PRIORS η ON THE DEEPLesion DATASET [43].

| Spectrum Prior | PSNR | SSIM |
|----------------------------------|-------------------|----------------------|
| Random Noise $\mathcal{N}(0, 1)$ | 22.45±4.64 | 0.8050±0.1529 |
| Noisy Spectrum (3%) | 35.64±1.48 | 0.9799±0.0063 |
| Noisy Spectrum (1.5%) | 36.80±1.26 | 0.9799±0.0063 |
| Clear Spectrum | 39.19±1.44 | 0.9844±0.0029 |

as available prior knowledge. Here, we study its influence on the model performance. Three types of spectra are compared. (1) Random Noise, a vector of length N sampled from the Gaussian distribution $\mathcal{N}(0, 1)$. (2) Noisy Spectrum, a spectrum corrupted by an additive noise following the Gaussian distribution $\mathcal{N}(0, \eta_{\max} \cdot c)$, where η_{\max} denotes the maximum values of the clear spectrum, and c is set to 3% and 1.5% to simulate two levels of noise. (3) Clear spectrum, *i.e.*, a GT spectrum. Table V shows the quantitative results. There are two observations. First, using the random noise as the energy spectrum causes severe degradation of the MAR performance, which decreases by 16.74 dB in terms of PSNR compared to using the clear spectrum. Second, the use of the noisy spectra decreases the performance of our Diner, but at an acceptable level. For example, the PSNR reaches 35.64 dB and 36.80 dB for the noisy spectra (1.5% and 3%). Figure 11 shows the qualitative results. From the visualization, we observe that the result of the noisy spectrum is significantly better than that of the random noise. In summary, the energy spectrum is required for our Diner, but it does not significantly affect the MAR performance if inaccurate.

3) *Influence of Discretization of Energy Spectrum*: The energy of a polychromatic X-ray physically covers a continuous range. However, due to limitations of physical instruments and numerical methods, measuring or estimating energy spectra are often based on discrete forms [42], [48], [49]. Our forward model \mathcal{T} also uses the discrete energy spectrum (Eq. (11)). Here, we discuss how this discretization affects the MAR performance. We set the energy range to [20, 120] KeV and then uniformly sample $N = \{1, 5, 10, 40, 81, 101\}$ energy levels from the range. Figure 12 shows the performance curve of our Diner over the discrete energy spectrum. From $N = 5$ to

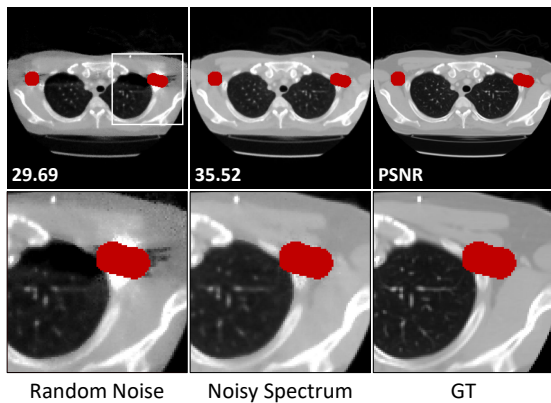


Fig. 11. Qualitative results of our Diner with two types of the X-ray energy spectra (random noisy and noisy spectrum) on a sample of the DeepLesion dataset [43]. The red regions denote metals.

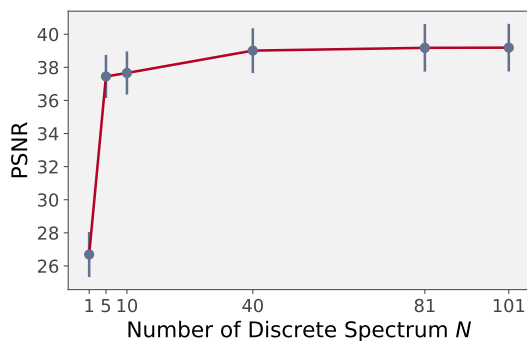


Fig. 12. Performance curve of our Diner with different discrete energy spectra $N = \{101, 81, 40, 10, 5, 1\}$ on the DeepLesion dataset [43]. Note that $N = 1$ means the degradation of the proposed forward model \mathcal{T} towards the linear integral model (Eq. (2)).

$N = 101$, the model performance remains excellent and robust (the change of the PSNR is less than 2 dB). When N is set to 1, our Diner fails to produce good results (PSNR is only about 27 dB). This is because the forward model \mathcal{T} degrades to a linear integral model (Eq. (3)) when $N = 1$, in which the energy-induced BHE cannot be handled. The qualitative results are shown in Figure 13. Visually, the MAR reconstruction is satisfactory in both local details and global structures when $N = 40$, while it contains several metal artifacts when $N = 1$. In summary, the MAR performance of our Diner is not affected by the discretization of the energy spectrum.

G. Failure Cases

Our Diner proposes a novel nonlinear forward model \mathcal{T} (Eq. (12)) to account for the complex BHE. However, there is another challenge when imaging objects containing ultra-high absorption metals, such as gold. As shown in Figure 14a, the X-rays hitting the ultra-high absorption metals are almost absorbed, resulting in the loss of valid measurement signals at the corresponding locations of the detectors. This phenomenon is called the photon starvation effect. Figure 14b shows a simulated gold-corrupted CT measurement, where the red regions represent the invalid signals and are background noise.

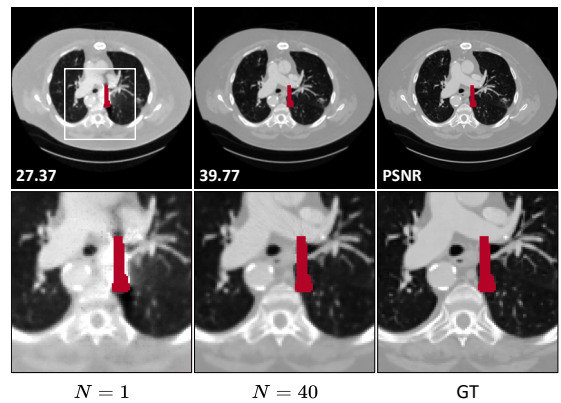


Fig. 13. Qualitative results of our Diner with two discrete energy spectra $N = \{1, 40\}$ on a sample of the DeepLesion dataset [43]. Note $N = 1$ means the degradation of the proposed forward model \mathcal{T} towards the linear integral model (Eq. (2)). The red regions denote metals.

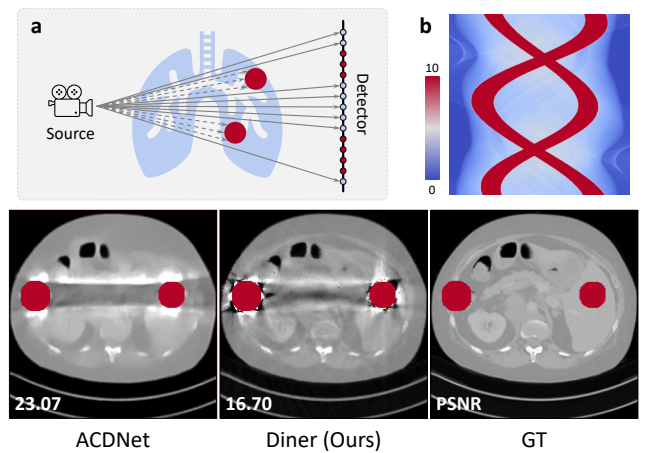


Fig. 14. A failure case of our Diner for ultra-high absorption metals. (a) A schema of the photon starvation effect, (b) A simulated gold-corrupted CT measurement on the DeepLesion [43] dataset, and (bottom row) Qualitative and quantitative results of ACDNet [9] and our Diner for the gold-corrupted measurement. The red regions denote metals.

However, our Diner considers the entire measurements as valid signals and uses them to optimize the INR network, causing the gradient error propagation. We show the MAR reconstructions by the SOTA-supervised ACDNet [9] and our Diner for the gold-corrupted CT measurement in Figure 14 (bottom row). Visually, the results of both techniques contain severe shadow artifacts and are unacceptable image quality. In summary, our Diner fails to handle the photon starvation effect caused by the ultra-high absorption metals. Nevertheless, we would like to emphasize that the common medical metal implants (*e.g.*, titanium, chromium, and 304 stainless steel) do not absorb X-rays as well as gold. Therefore, the proposed approach works for most clinical scenarios.

V. CONCLUSION AND LIMITATION

We present Diner, a novel reconstruction technique based on neural representation, to address the challenging MAR problem from a nonlinear perspective. The proposed Diner is fully unsupervised and thus does not require any external

training data, significantly enabling its usefulness in a wide of clinical scenarios. Our Diner learns a neural representation of the energy-independent densities of observed objects to handle the nonlinear BHE fundamentally. Extensive comparisons with popular MAR approaches and ablation studies confirm the effectiveness and reliability of the proposed method.

Although our Diner shows great potential for the MAR problem, several underlying limitations exist. For example, our Diner requires basic CT acquisition information, such as acquisition geometry and raw measurement data. However, the information might be inaccessible on clinical CT scanners due to commercial privacy.

REFERENCES

- [1] J. K. Seo and E. J. Woo, *Nonlinear inverse problems in imaging*. John Wiley & Sons, 2012.
- [2] A. C. Kak and M. Slaney, *Principles of computerized tomographic imaging*. SIAM, 2001.
- [3] L. Gjestebj, B. De Man, Y. Jin, H. Paganetti, J. Verburg, D. Giantsoudi, and G. Wang, “Metal artifact reduction in ct: where are we after four decades?,” *Ieee Access*, vol. 4, pp. 5826–5849, 2016.
- [4] W. A. Kalender, R. Hebel, and J. Ebersberger, “Reduction of ct artifacts caused by metallic implants,” *Radiology*, vol. 164, no. 2, pp. 576–577, 1987.
- [5] E. Meyer, R. Raupach, M. Lell, B. Schmidt, and M. Kachelrieß, “Normalized metal artifact reduction (nmar) in computed tomography,” *Medical physics*, vol. 37, no. 10, pp. 5482–5493, 2010.
- [6] R. Gordon, R. Bender, and G. T. Herman, “Algebraic reconstruction techniques (art) for three-dimensional electron microscopy and x-ray photography,” *Journal of theoretical Biology*, vol. 29, no. 3, pp. 471–481, 1970.
- [7] Y. Zhang and H. Yu, “Convolutional neural network based metal artifact reduction in x-ray computed tomography,” *IEEE transactions on medical imaging*, vol. 37, no. 6, pp. 1370–1381, 2018.
- [8] W.-A. Lin, H. Liao, C. Peng, X. Sun, J. Zhang, J. Luo, R. Chellappa, and S. K. Zhou, “Dudonet: Dual domain network for ct metal artifact reduction,” in *Proceedings of the IEEE/CVF Conference on Computer Vision and Pattern Recognition*, pp. 10512–10521, 2019.
- [9] H. Wang, Y. Li, D. Meng, and Y. Zheng, “Adaptive convolutional dictionary network for ct metal artifact reduction,” in *The 31st International Joint Conference on Artificial Intelligence*, IEEE, 2022.
- [10] H. Wang, Y. Li, N. He, K. Ma, D. Meng, and Y. Zheng, “Diednet: Deep interpretable convolutional dictionary network for metal artifact reduction in ct images,” *IEEE Transactions on Medical Imaging*, vol. 41, no. 4, pp. 869–880, 2021.
- [11] H. Liao, W. Lin, S. K. Zhou, and J. Luo, “Adn: Artifact disentanglement network for unsupervised metal artifact reduction,” *IEEE Transactions on Medical Imaging*, 2019.
- [12] L. Yu, Z. Zhang, X. Li, and L. Xing, “Deep sinogram completion with image prior for metal artifact reduction in ct images,” *IEEE transactions on medical imaging*, vol. 40, no. 1, pp. 228–238, 2020.
- [13] J. Wang, Y. Zhao, J. H. Noble, and B. M. Dawant, “Conditional generative adversarial networks for metal artifact reduction in ct images of the ear,” in *Medical Image Computing and Computer Assisted Intervention–MICCAI 2018: 21st International Conference, Granada, Spain, September 16–20, 2018, Proceedings, Part I*, pp. 3–11, Springer, 2018.
- [14] N. Rahaman, A. Baratin, D. Arpit, F. Draxler, M. Lin, F. Hamprecht, Y. Bengio, and A. Courville, “On the spectral bias of neural networks,” in *International Conference on Machine Learning*, pp. 5301–5310, PMLR, 2019.
- [15] Z.-Q. J. Xu, Y. Zhang, T. Luo, Y. Xiao, and Z. Ma, “Frequency principle: Fourier analysis sheds light on deep neural networks,” *arXiv preprint arXiv:1901.06523*, 2019.
- [16] L. Shen, J. Pauly, and L. Xing, “Nerp: implicit neural representation learning with prior embedding for sparsely sampled image reconstruction,” *IEEE Transactions on Neural Networks and Learning Systems*, 2022.
- [17] Q. Wu, R. Feng, H. Wei, J. Yu, and Y. Zhang, “Self-supervised coordinate projection network for sparse-view computed tomography,” *IEEE Transactions on Computational Imaging*, vol. 9, pp. 517–529, 2023.
- [18] Y. Sun, J. Liu, M. Xie, B. Wohlberg, and U. S. Kamilov, “Coil: Coordinate-based internal learning for tomographic imaging,” *IEEE Transactions on Computational Imaging*, vol. 7, pp. 1400–1412, 2021.
- [19] Q. Wu, X. Li, H. Wei, J. Yu, and Y. Zhang, “Joint rigid motion correction and sparse-view ct via self-calibrating neural field,” in *2023 IEEE 20th International Symposium on Biomedical Imaging (ISBI)*, pp. 1–5, IEEE, 2023.
- [20] G. Zang, R. Idoughi, R. Li, P. Wonka, and W. Heidrich, “Intratomo: self-supervised learning-based tomography via sinogram synthesis and prediction,” in *Proceedings of the IEEE/CVF International Conference on Computer Vision*, pp. 1960–1970, 2021.
- [21] R. Zha, Y. Zhang, and H. Li, “Naf: Neural attenuation fields for sparse-view cbct reconstruction,” in *Medical Image Computing and Computer Assisted Intervention–MICCAI 2022: 25th International Conference, Singapore, September 18–22, 2022, Proceedings, Part VI*, pp. 442–452, Springer, 2022.
- [22] D. Rückert, Y. Wang, R. Li, R. Idoughi, and W. Heidrich, “Neat: Neural adaptive tomography,” *ACM Transactions on Graphics (TOG)*, vol. 41, no. 4, pp. 1–13, 2022.
- [23] Z. Chen, K. Gupta, and F. Contijoch, “Motion correction image reconstruction using neuralct improves with spatially aware object segmentation,” in *7th International Conference on Image Formation in X-Ray Computed Tomography*, vol. 12304, pp. 276–281, SPIE, 2022.
- [24] K. Gupta, B. Colvert, Z. Chen, and F. Contijoch, “Difir-ct: Distance field representation to resolve motion artifacts in computed tomography,” *Medical Physics*, vol. 50, no. 3, pp. 1349–1366, 2023.
- [25] A. W. Reed, H. Kim, R. Anirudh, K. A. Mohan, K. Champley, J. Kang, and S. Jayasuriya, “Dynamic ct reconstruction from limited views with implicit neural representations and parametric motion fields,” in *Proceedings of the IEEE/CVF International Conference on Computer Vision*, pp. 2258–2268, 2021.
- [26] Q. Wu, L. Chen, C. Wang, H. Wei, S. K. Zhou, J. Yu, and Y. Zhang, “Unsupervised polychromatic neural representation for ct metal artifact reduction,” in *Advances in Neural Information Processing Systems (A. Oh, T. Neumann, A. Globerson, K. Saenko, M. Hardt, and S. Levine, eds.)*, vol. 36, pp. 69605–69624, Curran Associates, Inc., 2023.
- [27] J. H. Lambert, *Photometria sive de mensura et gradibus luminis, colorum et umbrae*. Klett, 1760.
- [28] A. Beer, “Bestimmung der absorption des rothen lichts in farbigen flussigkeiten,” *Ann. Physik*, vol. 162, pp. 78–88, 1852.
- [29] C. Shannon, “Communication in the presence of noise,” *Proceedings of the IRE*, vol. 37, no. 1, pp. 10–21, 1949.
- [30] M. J. Berger, J. H. Hubbell, S. M. Seltzer, J. Chang, J. S. Coursey, R. Sukumar, D. S. Zucker, and K. Olsen, “Xcom: Photon cross section database (version 1.5).” Online, 2010. Available: <http://physics.nist.gov/xcom> [July 24, 2023].
- [31] L. I. Rudin, S. Osher, and E. Fatemi, “Nonlinear total variation based noise removal algorithms,” *Physica D: nonlinear phenomena*, vol. 60, no. 1–4, pp. 259–268, 1992.
- [32] Y. Song, L. Shen, L. Xing, and S. Ermon, “Solving inverse problems in medical imaging with score-based generative models,” in *International Conference on Learning Representations*, 2022.
- [33] A. McNair, “Icru report 33-radiation quantities and units pub: International commission on radiation units and measurements, washington dc usa issued 15 april 1980, pp. 25,” 1981.
- [34] J. Beutel, *Handbook of medical imaging*, vol. 3. Spie Press, 2000.
- [35] H. Huang and S. Wu, “The evaluation of mass densities of the human body in vivi from ct scans,” *Computers in Biology and Medicine*, vol. 6, no. 4, pp. 337–343, 1976.
- [36] W. Geraldelli, A. Tomal, and M. E. Poletti, “Characterization of tissue-equivalent materials through measurements of the linear attenuation coefficient and scattering profiles obtained with polyenergetic beams,” *IEEE Transactions on Nuclear Science*, vol. 60, no. 2, pp. 566–571, 2013.
- [37] J. H. Hubbell and S. M. Seltzer, “Tables of x-ray mass attenuation coefficients and mass energy-absorption coefficients (version 1.4).” Online, 2004. Available: <http://physics.nist.gov/xaamdi> [2004, July 12].
- [38] V. Sitzmann, J. Martel, A. Bergman, D. Lindell, and G. Wetzstein, “Implicit neural representations with periodic activation functions,” *Advances in neural information processing systems*, vol. 33, pp. 7462–7473, 2020.
- [39] B. Mildenhall, P. P. Srinivasan, M. Tancik, J. T. Barron, R. Ramamoorthi, and R. Ng, “Nerf: Representing scenes as neural radiance fields for view synthesis,” *Communications of the ACM*, vol. 65, no. 1, pp. 99–106, 2021.
- [40] M. Tancik, P. Srinivasan, B. Mildenhall, S. Fridovich-Keil, N. Raghavan, U. Singhal, R. Ramamoorthi, J. Barron, and R. Ng, “Fourier features let networks learn high frequency functions in low dimensional domains,” *Advances in Neural Information Processing Systems*, vol. 33, pp. 7537–7547, 2020.

- [41] T. Müller, A. Evans, C. Schied, and A. Keller, "Instant neural graphics primitives with a multiresolution hash encoding," *ACM Trans. Graph.*, vol. 41, jul 2022.
- [42] J. Punnoose, J. Xu, A. Sisniega, W. Zbijewski, and J. Siewerdsen, "Technical note: spektr 3.0—a computational tool for x-ray spectrum," *Medical Physics*, vol. 43, no. 8, pp. 4711–4717, 2016.
- [43] K. Yan, X. Wang, L. Lu, L. Zhang, A. P. Harrison, M. Bagheri, and R. M. Summers, "Deep lesion graphs in the wild: relationship learning and organization of significant radiology image findings in a diverse large-scale lesion database," in *Proceedings of the IEEE Conference on Computer Vision and Pattern Recognition*, pp. 9261–9270, 2018.
- [44] S. G. Armato III, G. McLennan, L. Bidaut, M. F. McNitt-Gray, C. R. Meyer, A. P. Reeves, B. Zhao, D. R. Aberle, C. I. Henschke, E. A. Hoffman, *et al.*, "The lung image database consortium (lidc) and image database resource initiative (idri): a completed reference database of lung nodules on ct scans," *Medical physics*, vol. 38, no. 2, pp. 915–931, 2011.
- [45] D. P. Kingma and J. Ba, "Adam: A method for stochastic optimization," *CoRR*, vol. abs/1412.6980, 2015.
- [46] Z. Wang, A. C. Bovik, H. R. Sheikh, and E. P. Simoncelli, "Image quality assessment: from error visibility to structural similarity," *IEEE transactions on image processing*, vol. 13, no. 4, pp. 600–612, 2004.
- [47] S. van der Walt, J. L. Schönberger, J. Nunez-Iglesias, F. Boulogne, J. D. Warner, N. Yager, E. Gouillart, T. Yu, and the scikit-image contributors, "scikit-image: image processing in Python," *PeerJ*, vol. 2, p. e453, 6 2014.
- [48] J. M. Boone and J. A. Seibert, "An accurate method for computer-generating tungsten anode x-ray spectra from 30 to 140 kv," *Medical physics*, vol. 24, no. 11, pp. 1661–1670, 1997.
- [49] G. Poludniowski, G. Landry, F. Deblois, P. Evans, and F. Verhaegen, "Spekcalc: a program to calculate photon spectra from tungsten anode x-ray tubes," *Physics in Medicine & Biology*, vol. 54, no. 19, p. N433, 2009.



Qing Wu (Graduate Student Member, IEEE) received the B.Eng. degree in Communications Engineering from China University of Geosciences, Wuhan, China, in 2020. He is currently pursuing the Ph.D. degree in ShanghaiTech University, Shanghai, China. His current research interests include medical image reconstruction and implicit neural representation.



Xu Guo received the B.S. degree in Animal Science from Northwest AF University, Shaanxi, China, in 2021. She is currently pursuing the M.S. degree in ShanghaiTech University, Shanghai, China. Her current research interests include macrophage-stem cell interaction and fracture healing.



Lixuan Chen received the B.Eng. degree in Computer Science and Technology from ShanghaiTech University, Shanghai, China, in 2021. She is currently pursuing the M.S. degree in ShanghaiTech University, Shanghai, China. Her current research interests include medical imaging, deep learning, and image processing.



DongMing He currently works at the Department of Oral and Craniomaxillofacial Surgery, Shanghai Ninth People's Hospital as an attending surgeon, and carrying out researches at Shanghai Key Laboratory of Stomatology, Shanghai, China. He received his Ph.D. degree from West China School of Stomatology, SiChuan University (SCU) in 2018. His research focuses on biomaterials, regenerative medicine, and digital surgical technology.



mapping.

Hongjiang Wei received the B.Eng. degree from the Department of Electronic Information Engineering, Harbin Institute of Technology, Harbin, China, in 2008, the M.Sc. degree from the Department of Electronic Information Engineering, Harbin Institute of Technology, in 2010, and the Ph.D. degree from the Institute National des Sciences Appliquees de Lyon, Lyon, France, in 2014. He is currently with the School of Biomedical Engineering of Shanghai Jiao Tong University, Shanghai, China, specializing in fast MRI, deep learning, and quantitative susceptibility



and distraction osteogenesis for the difficult congenital or acquired dental and maxillofacial malformations. He has published 139 papers, more than 40 authorized patents.

Xudong Wang M.D., Chief Physician. He is currently the vice president of the Ninth People's Hospital affiliated with Shanghai Jiaotong University School of Medicine, the chairman of the Oral and Maxillofacial Trauma and Orthognathic Specialized Committee of the Chinese Stomatological Association, and the vice president of the Council of Precision and Digital Medicine Branch of the Chinese Society of Plastic and Aesthetic Surgery. He is mainly engaged in the research of the precision and minimally invasive treatments of orthognathic surgery



and peer-reviewed journal and conference papers, registered 140+ granted patents, written three research monographs, and edited three books. The two recent books he led the edition are entitled "Deep Learning for Medical Image Analysis, SK Zhou, H Greenspan, DG Shen (Eds.)" and "Handbook of Medical Image Computing and Computer Assisted Intervention, SK Zhou, D Rueckert, G Fichtinger (Eds.)". He has won multiple awards including R&D 100 Award (Oscar of Invention), Siemens Inventor of the Year, UMD ECE Distinguished Alumni Award, BMEF Editor of the Year, Finalist Paper for MICCAI Young Scientist Award (twice). He has been a program co-chair for MICCAI 2020, an associate editor for IEEE TRANSACTIONS ON MEDICAL IMAGING, IEEE TRANSACTIONS ON PATTERN ANALYSIS AND MACHINE INTELLIGENCE, and *Medical Image Analysis*, and an area chair for AAAI, CVPR, ICCV, MICCAI, and NeurIPS. He has been elected as a treasurer and board member of the MICCAI Society, an advisory board member of MONAI (Medical Open Network for AI), and a fellow of AIMBE, IAMBE, IEEE, MICCAI, and NAI (National Academy of Inventors).

S. Kevin Zhou (Fellow, IEEE) received his PhD degree from University of Maryland, College Park. Currently he is a distinguished professor and founding executive dean of School of Biomedical Engineering, University of Science and Technology of China (USTC) and an adjunct professor at Institute of Computing Technology, Chinese Academy of Sciences and Chinese University of Hong Kong (CUHK), Shenzhen. Prior to this, he was a principal expert and a senior R&D director at Siemens Healthcare Research. Dr. Zhou has published 250+ book chapters



Yifeng Zhang received his bachelor's degree in Clinical Medicine in Shanxi Medical University in 2006. In 2007, he studied nanomaterials' biosafety in College of Engineering, Peking University, and received his master's degree in Biomedical Engineering in 2010. Then, he did the researches about the mechanism of Mg's osteogenesis effect in Prince of Wales Hospital, The Chinese University of Hong Kong in 2011. In 2015, Dr. Zhang obtained his PhD degree. From 2015 to 2019, Dr Zhang explored several biomedical directions based on Mg ions'

bioactivities, such as bone fracture repair, osteoarthritis, tendon repair, et al. in School of Medicine, Nanjing University. In 2019, Dr. Zhang joined in School of Life Science and Technology, ShanghaiTech University, and established research group of Sports Medicine.



Jingyi Yu (Fellow, IEEE) received BS from Caltech in 2000 and the Ph.D. degree from MIT in 2005. He is currently the Vice Provost at ShanghaiTech University. Before joining ShanghaiTech, he was a full professor in the Department of Computer and Information Sciences at University of Delaware. His research interests span a range of topics in computer vision and computer graphics, especially on computational photography and nonconventional optics and camera designs. He is a recipient of the NSF CAREER Award and the AFOSR YIP

Award, and has served as an area chair of many international conferences including CVPR, ICCV, ECCV, IJCAI and NeurIPS. He was a program chair of CVPR 2021 and will be a program chair of ICCV 2025. He has been an associate editor of IEEE TRANSACTIONS ON PATTERN ANALYSIS AND MACHINE INTELLIGENCE. He is currently an associate editor of IEEE TRANSACTIONS ON IMAGE PROCESSING, and *Elsevier Computer Vision and Image Understanding*. He is a fellow of IEEE.



Yuyao Zhang (Member, IEEE) received the B.Eng. degree from the Department of Electronic Information Engineering, Harbin Engineering University, Harbin, China, in 2007 and the M.Sc. degree from the Department of Electronic Information Engineering, Harbin Institute of Technology, Harbin, in 2010, and the Ph.D. degree from the Institut National des Sciences Appliquees de Lyon, Lyon, France, in 2014. She currently works in School of Information Science and Technology of Shanghaitech University, specializing in medical image processing.